Available online at www.sciencedirect.com

ScienceDirect

Geochimica et Cosmochimica Acta 280 (2020) 116–129

Geochimica et Cosmochimica Acta

www.elsevier.com/locate/gca

Ion specific effects on the pressure solution of calcite single crystals

Yijue Diao [a], Anqi Li [a], Rosa M. Espinosa-Marzal [a,b,*]

[a] Civil and Environmental Engineering, University of Illinois at Urbana-Champaign, 205 N. Matthews Avenue, Urbana, IL 61801, United States
[b] Materials Science and Engineering, University of Illinois at Urbana-Champaign, 1304 W Green St, Urbana, IL 61801, United States

Received 6 August 2019; accepted in revised form 8 April 2020; available online 17 April 2020

Abstract

Pressure solution of carbonate-based rocks participates in many geophysical and geochemical processes occurring at or near the Earth's surface, but fundamental knowledge is still lacking. Here, the pressure solution of calcite single crystals in water, NaCl and $CaCl_2$ brines was investigated with an extended surface forces apparatus (SFA). This highly mechanically and thermally stable measuring technique enables to measure the deformation of two single calcite crystals undergoing pressure solution and the deformation rates with high precision as a function of load and fluid composition. The measurements in water reveal both diffusion- and dissolution-limited scenarios. Further, the pressure solution of calcite decelerates with a small concentration of NaCl compared to $CaCO_3$-saturated solution, while the rate is promoted with an increase to 100 mM NaCl, reflecting the competition of at least two different mechanisms. In contrast, the addition of small concentrations of $CaCl_2$ already speeds up calcite's pressure solution. These experimental results cannot be solely explained *via* the increase in solubility of calcite with ionic strength, as generally proposed. Instead, they are consistent with the ion-specific effects of the interfacial composition and the distortion of the hydration structure of calcite under an applied pressure smaller than ~25 MPa. This work advances the fundamental knowledge of pressure solution of calcite. More broadly, the novel technique developed here can be applied to other brittle and unexfoliable minerals, which notably expands the applications of SFA.

Keywords: Calcite; Pressure solution; Interfacial properties; Nanoconfinement; Surface forces apparatus

1. INTRODUCTION

Contact stresses applied on mineral surfaces enhance the chemical potential of the stressed solid and thereby its solubility above that of the stress-free mineral. As a result of the local increase in solubility, the dramatic undersaturation of the interfacial solution leads to mineral dissolution. The dissolved mineral diffuses through the fluid film confined at grain boundaries, and subsequently reprecipitates in stress-free or less stressed regions nearby. This process of dissolution, diffusion, and reprecipitation is called pressure solution (Weyl, 1959). Pressure solution of minerals is the major mechanism of ductile deformation of the Earth's upper crust (Gratier et al., 2013), and plays a critical role in a variety of geological processes, such as diagenesis (Gundersen et al., 2002) and interseismic fault healing (Chester and Higgs, 1992). It is therefore crucial to understand the mechanisms underlying pressure solution.

Carbonate-based rocks abound in lithosphere and are reactive in aqueous environment. A number of studies have focused on the pressure solution of calcite (Gratier et al., 2013), which is the most stable crystalline polymorph of calcium carbonate. Measurements of indentation depth on single crystals under a dead weight has been applied to study pressure solution of minerals (Rutter and Elliott, 1976; Gratier et al., 2013), including (to the best of our knowledge) two studies on calcite (Zubtsov et al., 2005; Croizé

* Corresponding author at: Civil and Environmental Engineering, University of Illinois at Urbana-Champaign, 205 N. Matthews Avenue, Urbana, IL 61801, United States.
E-mail address: rosae@illinois.edu (R.M. Espinosa-Marzal).

https://doi.org/10.1016/j.gca.2020.04.010
0016-7037/

et al., 2010). The advantage of this experimental approach is that the "true" contact area (of micrometer size) can be visualized, which facilitates understanding the underlying mechanisms. However, the experiment duration is typically long, usually weeks or even months, during which the measurement's accuracy is unfortunately discounted. Using a capacitance dilatometer to significantly enhance the sensitivity of indentation measurements and reduce their duration, Zubtsov et al. (2005) investigated the pressure solution of calcite in ammonium chloride solutions at contact stresses ranging between 50 and 200 MPa. While the process was reported to be diffusion-limited, microcracks were observed, which could have contributed to the measured deformation. Croizé et al. (2010) used optical interferometry to achieve high precision in indentation measurements on calcite with glass and sapphire indenters. However, these experiments also led to the formation of microcracks and the rate-limiting step during calcite's pressure solution could not be determined. Dickinson et al. (1997) investigated the stress-induced dissolution of calcite *via* the visualization of the wear track made with an atomic force microscopy (AFM) tip while sliding along the mineral surface. The authors proposed that the high tensile stress (>1 GPa) around the tip led to the nucleation of double kinks, which served as pit nuclei and accelerated the dissolution of calcite. In either case, the asymmetric contact in indentation and AFM experiments do not fully resemble the grain boundaries found in natural systems.

Another experimental approach has focused on monitoring the strain rate of compacted granular calcite to investigate, for example, the effect of grain size and effective stress on pressure solution (Salemans et al., 2002; Zhang and Spiers, 2005a; Zhang and Spiers, 2005b). Here, the strain rate is correlated to the grain size by a power law whose exponent is associated with the rate limiting mechanism (Zhang and Spiers, 2005a). The role of fluid chemistry on the strain rate has been evidenced in a few works. For instance, the strain rate was observed to decrease by the addition of magnesium salts up to 1 molar (Salemans et al., 2002; Zhang and Spiers, 2005a) but it increased in 0.1 and 0.5 molar NaCl solutions (Zhang and Spiers, 2005a). In contrast, others observed a reduced strain rate of granular calcite in NaCl solutions of comparable and higher concentrations at higher effective stress (30 vs. 4 MPa) (Liteanu and Spiers, 2009). Microstructure analysis suggested that the strain rate should be considered as a combination of both the mechanical compaction facilitated by crack propagation, and the pressure solution creep (Croizé et al., 2010). While the rate of pressure solution is much faster here than in indentation measurements, and this reduces the experiment duration, the "true" contact area and contact stress cannot be explicitly quantified. Furthermore, the complexity of the system makes it challenging to unambiguously deconvolute pressure solution from other deformation mechanisms, such as plastic deformation (Verberne et al., 2013) and grain boundary sliding (Wheeler, 2010). These limitations call for more advanced approaches to investigate pressure solution mechanisms.

The surface forces apparatus (SFA) is conventionally used to measure colloidal forces between two mica sheets (of a few microns in thickness) conformed onto two cylindrical glass lenses. The silver serves as mirror to reflect the white light multiple times, while the transmitted interference results in fringes of equal chromatic order (FECOs) of high finesse that are translated to a surface separation with angstrom resolution (Israelachvili, 1973). Unlike mica, calcite cannot be exfoliated, and therefore, obtaining μm-thick calcite crystals for light transmission is difficult. To the best of our knowledge, two attempts have been made to study the interactions between calcite surfaces by SFA. In those works, polycrystalline surfaces were prepared either by atomic layer deposition (Dziadkowiec et al., 2018) or crystallization of amorphous calcium carbonate by heating (Chen et al., 2017), which led to roughness variations of two orders of magnitude and a large variability of the dissolution rate. In this work, we extend the SFA to study the pressure solution of calcite single crystals for the first time. The large contact area between the two crystals, along with the precision of the crystal-thickness measurement have enabled us to determine the influence of applied load and of fluid composition (NaCl and $CaCl_2$ with a wide range of geologically relevant concentrations) on the pressure solution of calcite single crystals.

2. MATERIALS AND METHODS

2.1. Sample preparation

Solutions of NaCl and $CaCl_2$ (purity>=99.0%, Sigma-Aldrich) were made at room temperature with ultrapure water (18.2 MΩ-cm resistivity) to achieve concentrations of 0 mM (no salt added), 1 mM, 10 mM, 100 mM, and 1 M, respectively. These solutions were then equilibrated with excessive calcite powder (purity>=99.0%, Sigma-Aldrich) to obtain $CaCO_3$-saturated saturation. The solution was then filtered to remove calcite particles and degassed to eliminate bubbles introduced during the filtering step. Prior to their use in SFA experiments, the solutions were re-equilibrated with the laboratory air and the two calcite crystals. The pH was measured before and after the experiments, and it is shown in Table S1. The equilibrium pH was also calculated with Visual MINTEQ 3.1, assuming equilibrium with atmosphere and calcite. The good agreement between experimental and calculated pH values confirms the equilibration of the solutions.

The preparation of the calcite single crystals for SFA measurements is schematically represented in Fig. 1a. A piece of calcite cleaved along the $(10\bar{1}4)$ plane was glued onto the sample holder of an Allied Multi-Prep system with DiamondBond glue, which is a non-residual glue dissolved in acetone. The other side of the calcite crystal was polished down to ~20 μm with a surface roughness lower than 2 nm, confirmed by AFM tapping mode in a 1x1 μm^2 area. The Multi-prep system was calibrated to ensure the polished surface is as parallel as possible to the cleavage plane (angle < 0.001°). The mechanically polished side of the calcite piece was coated with 35-nm-thick silver. The calcite piece was then released from the holder by heating the glue to 150 °C and then intentionally broken into two smaller pieces with approximately the same thickness (difference

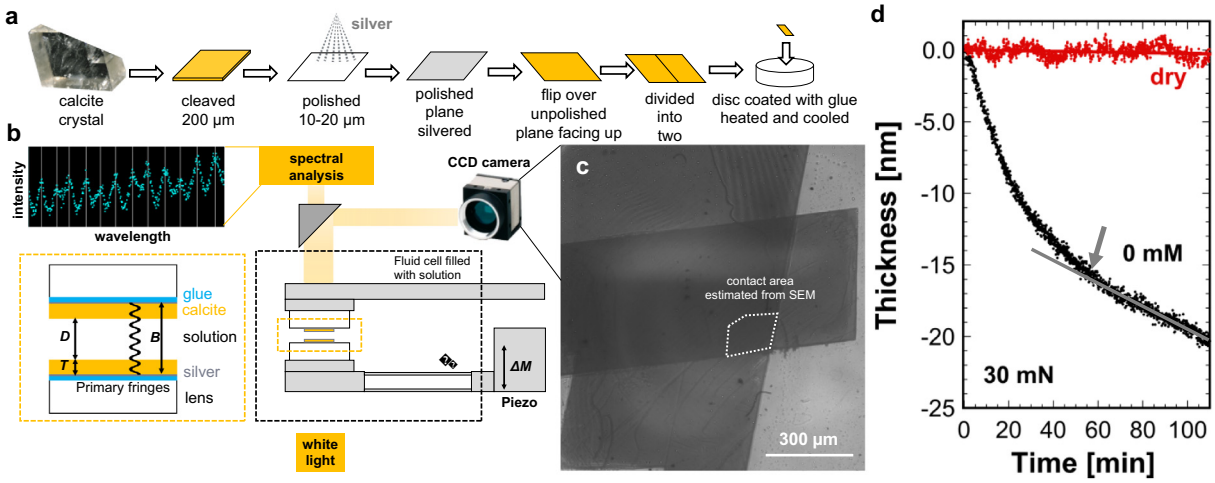

Fig. 1. (a) Sample preparation and (b) schematics of the setup. The applied load is calculated *via* the Hooke's law as $F = k_n \Delta M$, where ΔM is the distance traveled by the piezo from the point of contact between the calcite crystals and k_n is the spring constant. On the top right of (b), a representative transmitted spectrum for distance determination by Fast Spectral Correlation (Heuberger, 2001) is shown. The spectral analysis provides the distance between the two silver mirrors (B), which is the sum of the thickness of the two crystals ($2T$) and of the surface separation$D$. (c) Image of two calcite crystals taken with a Charge-Coupled Device (CCD) camera coupled with the SFA. (d) Measured change of the thickness of calcite crystals over time in dry nitrogen environment (red) and in calcium carbonate saturated solution (0 mM, black) at an applied load of 30 mN. The initial pressure solution in 0 mM solution (black) is faster than in steady-state, shown by the solid line. The pressure solution rates presented in following diagrams correspond to steady-state rates.

< 100 nm, quantified by profilometry). The silvered calcite surfaces were then glued onto the center of two flat glass lenses with the cleaved $(10\bar{1}4)$ plane upwards. They were then gently rinsed with excessive amounts of acetone and with water that had been previously equilibrated with calcium carbonate ($CaCO_3$) at 25 °C, three times with each, before blow-dried with dry nitrogen. To ensure that the cleaning step with acetone did not affect the surface properties of calcite, we measured the adhesion between a silicon tip and the cleaved $(10\bar{1}4)$ plane of calcite in dry nitrogen by AFM. The adhesion of calcite, washed following this cleaning protocol, was averaged over 100 measurements and compared to that of pristine calcite. A small increase in adhesion (2.88±0.54 vs. 2.12±0.47 nN) was observed due to the exposure to acetone, which is considered to be acceptable.

2.2. Pressure Solution Experiments by Surface Forces Apparatus

An extended SFA (abbreviated here as eSFA) was used in this work (Heuberger, 2001). The eSFA uses Fast Spectral Correlation (FSC), a fast and accurate numerical tool to analyze multilayer beam interferometry (MBI) spectra in real time (Heuberger, 2001). A detailed description of the interferometric analysis can be found in the SI. As in the traditional SFA, one glass lens holder is rigid, and the other one is attached to a spring with calibrated spring constant (k_N) (Fig. 1b). The holder can be both moved coarsely with a micrometer and driven with subnanometer precision by a piezometric actuator (E-753, PI Instrument) in the direction toward the other surface to a known position (M). The spectral analysis of the transmitted light interference through the calcite crystals provides the distance (B) between the two silver mirrors at the selected measuring position. B is thus the sum of the thickness of the two crystals and the surface separation$D$ at this position. In the traditional SFA setup, the mica thickness (T_0) remains constant, since mica is effectively insoluble in water. Therefore, the surface separation is obtained by subtracting the thickness of the mica sheets from B, *i.e.* ($D = B - 2T_0$). In pressure solution experiments, the thickness of the crystals (T) changes. The numeric algorithm that analyzes the light transmission cannot determine D and T simultaneously yet. However, D is expected to remain constant during pressure solution under steady-state conditions. Thus, the interferometric measurement of B provides the change in crystal thickness ΔT of the two calcite crystals in real time averaged within an area with a diameter of ~ 2 μm. The principle refractive index of calcite$n = 1.66$ was used in the analysis and the effect of the dispersion on the measurement of the crystal thickness was proved to be negligible in pressure-solution experiments (see error estimations in the SI). It is to be noted that the calcite thickness (~20 μm) is unavoidably much larger than that of the mica sheets (~3–5 μm) used in conventional SFA measurements. This results in more scattered data, see e.g. Fig. 2a. Nevertheless, the data scattering is usually smaller than 1 nm, yielding a standard deviation of ~ ±5 Å.

Since calcite is brittle, it does not allow the conventional cylinder-cylinder geometry of SFA experiments, but instead a plane-plane geometry is required. The challenging assembly of the calcite planes parallel to each other was carried

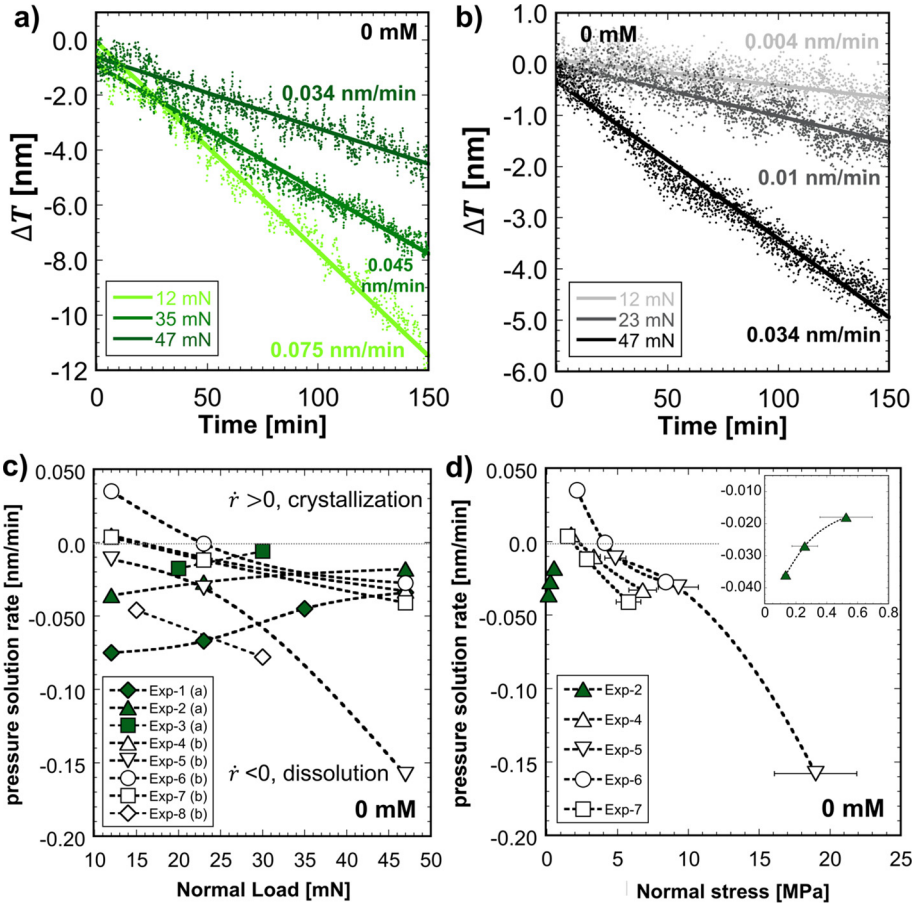

Fig. 2. (a-b) Representative SFA measurements of the change in crystal thickness (ΔT) in calcium carbonate ($CaCO_3$) saturated solution (denoted as 0 mM) as a function of applied load. The decrease in thickness, *i.e.*, given as$\Delta T < 0$, indicates dissolution, and the inverse ($\Delta T > 0$), indicates crystallization; the slope of the linear fit to the experimental data (solid lines) gives the dissolution and crystallization rate, respectively. The labels give the corresponding load; an increase in color intensity indicates increase in applied load. (a) and (b) represent the two observed scenarios. The dissolution rate decreases (less negative) with applied load in a), and it increases (more negative) with applied load in (b). The dissolution rate was found to be faster at the beginning of each experiment (Fig. 1d) and eventually achieved a steady state; we show the steady-state values here. A collection of the measured rates in 8 experiments with different pairs of calcite crystals is shown in (c). Positive and negative rates indicate precipitation and dissolution, respectively. Error bars, which show the root-mean-square error of the linear fits, are too small to be seen. Markers in green (full) and black shades (empty) are experiments similar to the scenario shown in (a) and (b), respectively. (d) Pressure-solution rates for selected experiments in (c) shown as a function of the normal stress, which was determined as the average between σ_n and σ_n^*, i.e. the final apparent and true contact stress, respectively. The inset shows an experiment corresponding to the scenario a.

out with the SFA located in the laminar flow hood (*ex situ*). Here, one of the flat lenses was brought close to the second lens with the coarse micrometer. Then, the top lens was slightly loosed from the holder to adjust its position until the two calcite surfaces gently touched each other. A magnifying lens was used to ensure the alignment of the crystals. After the SFA was secured in the thermally-controlled box, the fluid cell housing the glass lenses with the calcite crystals having their unpolished $(10\bar{1}4)$ cleavage plane facing each other was continuously purged with dry nitrogen of highest purity to avoid contamination. The surfaces were then manually brought into contact with extreme caution to avoid damage of the crystals. The alignment between the two crystals was then checked with a Charge-Coupled Device (CCD) camera (4000AM-T1-GE, DVC Company) coupled with the SFA *in situ* (Fig. 1c) and corrected if needed *ex situ*, as described above. The two crystals were visualized by the CCD camera in real-time during the measurement (Fig. 1c) so that any change of system geometry was rapidly detected during the measurement. The point of closest approach (PCA) becomes meaningless in a plane-plane geometry. Instead, by moving the spectrometer (Flame-S, Ocean Optics) in both X and Y directions with corresponding motors, the region at which the primary fringes are of highest quality was first roughly determined. Note that regions where the two calcite surfaces are not in contact yield a poorer interference than the contact region due to the larger separation between the mirrors.

The solution was slowly injected into the fluid cell until complete immersion of the calcite crystals. The experiments with each pair of crystals started with water equilibrated with $CaCO_3$ and then the concentration of either NaCl or $CaCl_2$ was increased stepwise. To ensure a thorough solution exchange, the two surfaces were first separated to$D > 10$ μm and then the liquid in the fluid cell was depleted and refilled 3 times with the new solution. The two calcite surfaces were brought into contact with the help of the micrometer. The initial crystal thickness T_0 was first roughly determined with the two calcite crystals in contact *via* MBI under the assumption that the two surfaces have the same thickness and the film thickness equals to zero (see details about the estimation of errors in the SI). To determine T_0 more precisely, the two surfaces were approached at 5 nm/s with the piezo, while the surface separation (D) was measured in real-time assuming constant $T = T_0$. When the change in the piezo position ΔM started to deviate from ΔD, the point of contact at zero load, M_0, was defined and the crystal thickness (T_0) was defined a the point of contact. 2D scans were performed again in search of the optimal spot for interferometric measurements, where the peak intensities are highest. Then the initial thickness T_0 was redefined at the point of contact. The two surfaces were then separated at 5 nm/s for 3-hr re-equilibration. This practice was repeated to re-define T_0 after each change in solution concentration, in case a change of crystal thickness happened during re-equilibration. The errors in the determination of calcite thickness stemming from the assumption of symmetry as well as $D = 0$ during pressure-solution are smaller than 0.2%, as demonstrated in the SI.

The piezo was moved to the position M at a constant velocity of 5 nm/s to apply the selected normal load, $F = k_n(M_0 - M)$. The thickness of the two calcite crystals ($2T$) upon an applied load was measured in real time and the change in thickness over time was used to calculate the pressure solution rate under steady-state conditions ($\Delta T/\Delta t$). The selected loads in this work (12, 23 and 47 mN) were probed for each selected concentration. In each solution, the normal load was decreased and increased to evaluate the reversibility of the pressure solution rate. It is to be noted that F changes during the pressure solution experiments, as the change of calcite thickness leads to a shift of the point of contact M_0. Over the duration of one experiment at constant concentration, the decrease in T is smaller than $\sim$ 50 nm, which leads to a change of the load of less than 0.1 mN. However, surface roughening can lead to significant variations of the local contact stress even at constant load. All SFA measurements were conducted at 25 ± 0.04 °C. It was confirmed that the thermal fluctuations (Fig. S4) did not interfere with the pressure solution measurements. Reference measurements also showed that thermal fluctuations are more pronounced in the dry nitrogen environment than upon immersion in aqueous solutions. The mechanical drift of the instrument was smaller than 0.005 nm/min. SFA experiments in $CaCO_3$ saturated solutions were performed on 8 different pairs of calcite crystals to demonstrate reproducibility, and the corresponding results are shown in Fig. 2c. Two replica experiments were carried out in each NaCl and $CaCl_2$ solution (see Fig. 4 and Fig. S5).

2.3. Scanning Electron Microscopy

Scanning Electron Microscopy (SEM) images were taken after each pressure solution experiment. Calcite samples were rinsed gently with nanopore water 3 times before blowing-dry with nitrogen. Drying of the sample in salt solutions was avoided. The samples were then fixed to a sample holder and coated with 5 nm Pd with a sputter coater (Emitech K-575). The coated samples were imaged with a SEM (Hitachi S-4700) at a vacuum of 10^{-5} torr, working distance of $\sim$ 12 mm, an acceleration voltage of 5–10 kV and an emission current of 5–10 μA. At the end of the experiment, the SEM images were used to visualize

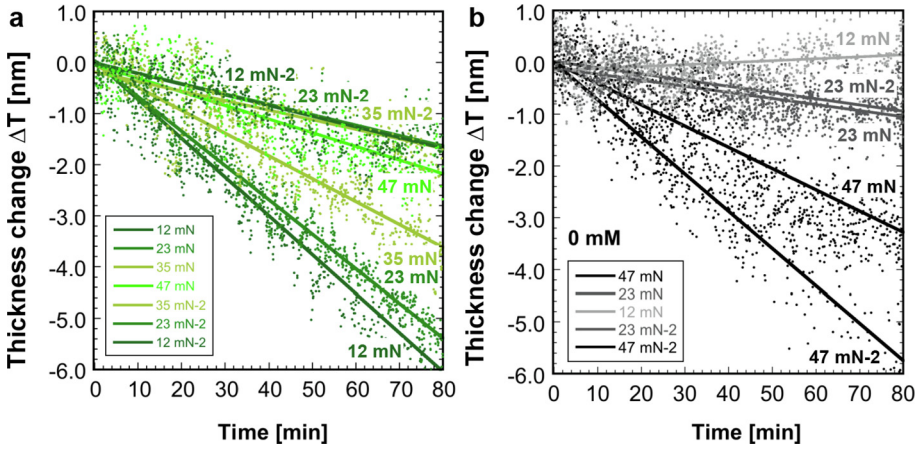

Fig. 3. Change of crystal thickness (ΔT) over time due to the pressure solution of calcite in calcium carbonate saturated solution (0 mM) during loading and unloading (labeled as "-2"). a) represents the scenario in Fig. 2a (green full markers in Fig. 2c and d), where an increase in load leads to a smaller pressure solution rate. (b) represents the scenario in Fig. 2b (black empty markers in Fig. 2c and d), where an increase in load leads to more prominent pressure solution rates.

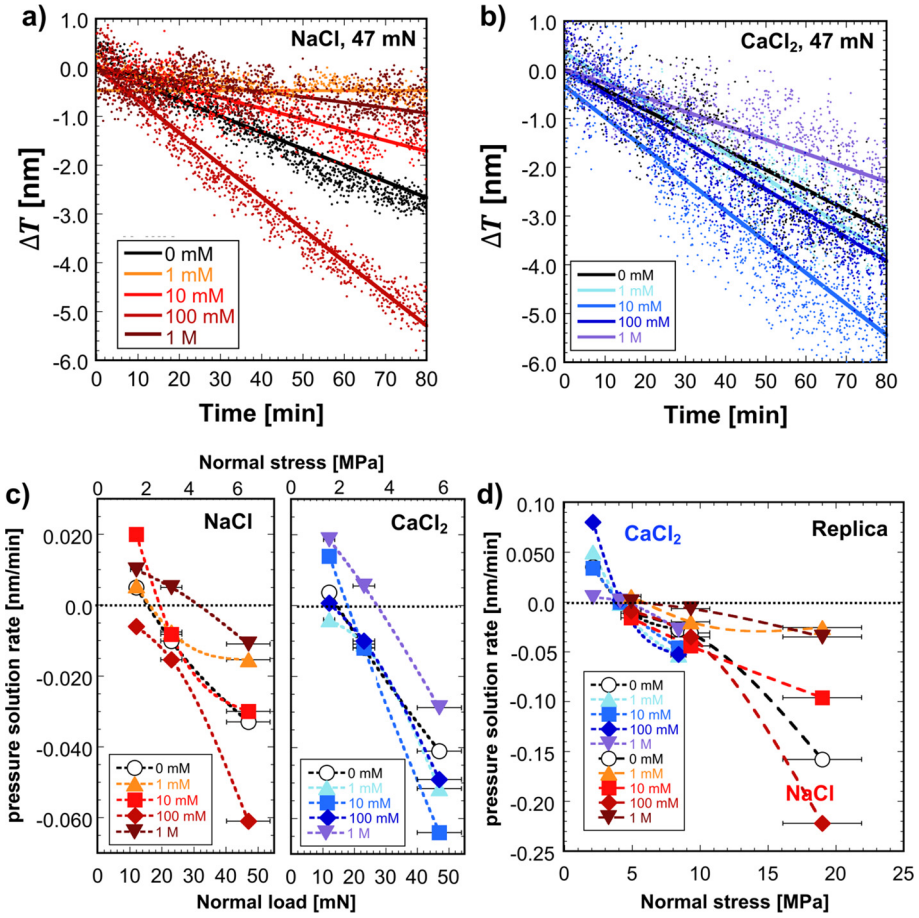

Fig. 4. Representative results for the pressure-solution rate as a function of concentration of (a) sodium chloride (NaCl), and (d) calcium chloride ($CaCl_2$) at an applied load of 47 mN. By imaging the contact area, the apparent normal stresses were estimated to be ~ 5–7 MPa (See Tables S5 and S6). (c) Summarizes the pressure-solution rate at three loads, namely, 12 mN, 23 mN, and 47 mN. The secondary X-axis shows the normal stress, determined as the average between σ_n and σ_n^*, i.e. final apparent and true contact stress, respectively. The error bars correspond to the stress, not to the load. (d) Pressure-solution rates in replica experiments of (a-b) shown as a function of the average between σ_n and σ_n^*. The error bars show the difference between σ_n and σ_n^*. The error bars for the $CaCl_2$ are smaller than the symbol size, and therefore, they cannot be seen in Fig. 4d. The experimental data are presented in Fig. S5.

the footprint of pressure solution and to determine the footprint area using the software ImageJ (https://imagej.nih.gov/ij/). The total area of the footprint is labeled as the apparent contact area (A). Because roughness developed during the pressure-solution experiments, the true contact area differs from the apparent contact area. Therefore, the contact stress changes during the course of the experiment, even if the load is maintained constant. In the SEM images, non-contact regions larger than a few microns were identified, and their area was subtracted from A to provide a rough estimate of the true contact area A^* at the end of the experiment. This is a rough estimation of the true contact area because the size of the single-asperity contacts could be smaller. The apparent normal stress $\sigma_n \sim F/A$, and the true contact stress $\sigma_n^* \sim F/A^*$, were both determined at the end of the SFA experiment, representing limits for the minimum and the maximum stress, respectively. The selected loads in this work are 12, 23 and 47 mN, which correspond to an apparent stress smaller than 25 MPa.

2.4. Nanoindentation

Freshly cleaved calcite crystals along the $(10\bar{1}4)$ plane were immersed in NaCl and $CaCl_2$ solutions at the selected concentrations of 0 mM (no added salt, $CaCO_3$-saturated solution), 1 mM, 10 mM, 100 mM, and 1 M. A NHT^3 nanoindentation tester (Anton Paar) with a Berkovich diamond tip (B-Q 62) was used in these experiments. The initial indentation due to elastic deformation was subtracted from the measured indentation depth. The indentation rate was determined with the indentation depth after 1.5 hours under the specified applied loads, namely, 50 mN, 100 mN, and 200 mN, which correspond to a normal stress ranging from 1 to 3 GPa, and hence, much higher than in the SFA experiments. After the indentation tests, SEM images of the indented region were taken to examine microcrack formation. The calcite crystals were gently rinsed with nanopore water three times and then blown-dry with nitrogen before SEM imaging.

3. RESULTS

3.1. Load-dependent pressure solution experiments in $CaCO_3$ saturated solutions

References SFA measurements under applied load showed no change of the crystal thickness in dry nitrogen (Fig. 1d). Only in the presence of solution, a change in crystal thickness (ΔT) was measured (saturated $CaCO_3$ solution in Fig. 1d) and attributed to the pressure solution of the single crystals. When a load was first applied on a fresh pair of calcite crystals with their cleavage planes pressed against each other, the initial dissolution rate was faster than under steady-state conditions (see solid line in Fig. 1d). Note that the varying dissolution rate in our experiments deviates from the reported scaling relation $\Delta T \sim \Delta t^{1/3}$, which has been associated with a coarsening of surface roughness during pressure-solution of calcite in indentation experiments (Dysthe et al., 2003b), and hence, we cautiosly exclude this mechanism. Instead, this observation is associated with the presence of a few terraces and kinks at the cleaved calcite surfaces, which leads to the formation of single asperity contacts between the two calcite surfaces and to higher stresses at the asperity contacts, which promote dissolution. The dissolution gradually slowed down until a constant dissolution rate was achieved (steady state). The pressure solution rates presented in this work correspond to steady-state conditions.

Fig. 2a-b show representative measurements of the change in crystal thickness over time at the three selected normal loads in calcium carbonate ($CaCO_3$) saturated solutions in steady state. The solid lines show the linear fit to the experimental data, and the slope gives the rate of pressure solution, negative and positive values representing dissolution and crystallization rates, respectively. The measured rates in experiments with different pairs of calcite crystals are summarized in Fig. 2c. Fig. 2a and 2b represent the two common scenarios. In (a), the higher the load, the slower the decrease in crystal thickness is, *i.e.*, the less negative the pressure-solution rate becomes. Out of eight experiments with different pairs of calcite crystals, three trials showed this pattern (full markers in Fig. 2c and d). In contrast, Fig. 2b shows the opposite trend, where the decrease in thickness speeds up with an increase in normal load. This trend was observed in five out of eight experiments with different pairs of calcite crystals (empty markers in Fig. 2c). Interestingly, an increase of the crystal thickness with time, *i.e.* crystallization, was occasionally measured at the lowest normal load of 12 mN, as illustrated by the positive rates.

The change of the pressure-solution rate upon increase and decrease in load was also examined. Fig. 3a represents the scenario in Fig. 2a (green full markers in Fig. 2c and d), where an increase in load leads to a smaller pressure solution rate. In this experiment, the applied load was first increased from 12 to 23 mN, and further to 35 and 47 mN, and then decreased from 47 to 35 mN and then further to 23 and 12 mN. The corresponding pressure solution rate is −0.076, −0.067, −0.045, −0.027, −0.020, −0.020 and −0.021 nm/min, respectively, reflecting the irreversibility of the pressure solution. In contrast, in Fig. 3b, representing the scenario in Fig. 2b (black empty markers in Fig. 2c and d), an increase in load leads to higher pressure-solution rates and *vice versa*. In this experiment, the applied load was first decreased from 47 to 23 mN, and further to 12 mN and then increased from 12 to 23 mN and further to 47 mN. The pressure solution rate is −0.05, −0.01, 0.004, −0.01, and −0.07 nm/min, respectively. That is, the pressure-solution rate reversed upon the increase in load in Fig. 3b, while this did not happen in Fig. 3a. It is to be noted that due to the roughening of the surface (shown later) during pressure solution, the contact area, and thereby both the true normal stress and the diffusion length are expected to vary over the course of the measurement and affect pressure solution. The observed changes in Fig. 3 are consistent with a more significant change in contact area in the scenario depicted in Fig. 3a compared to the scenario in Fig. 3b, as discussed later.

3.2. Pressure Solution Experiments in NaCl and $CaCl_2$ solutions

The influence of fluid chemistry on pressure solution was investigated by measuring the pressure-solution rates in NaCl and $CaCl_2$ solutions. Representative results in Fig. 4a-b from two different experiments illustrate that the thickness decreased in NaCl and $CaCl_2$ solutions at the applied load of 47 mN; other replica experiments are shown in Fig. S5. In NaCl (Fig. 4a), the pressure-solution rate slowed down from −0.033 nm/min to −0.01 nm/min upon the addition of 1 mM NaCl. When the concentration increased to 10 mM NaCl, the pressure-solution rate became faster (−0.21 nm/min), but it was still slower than in saturated $CaCO_3$ solution (0 mM). This increase in pressure-solution rate with concentration prevailed at 100 mM NaCl, at which the rate was roughly twice than at 0 mM. The pressure-solution rate decreased abruptly to −0.011 nm/min at the highest concentration of 1 M NaCl, showing a deviation from the behavior at smaller concentrations. These results are in remarkable contrast to the measured rates in $CaCl_2$ solutions, shown in Fig. 4b. Here, the pressure-solution rate gradually increased from −0.041 to −0.064 nm/min when the concentration of $CaCl_2$ was increased to 10 mM. Further increase of the concentration of $CaCl_2$ to 100 mM led to a small decrease in the pressure-solution rate to −0.05 nm/min but it remained still higher than at 0 mM, while it was further reduced to −0.028 nm/min in 1 M $CaCl_2$.

The pressure solution of calcite in NaCl and $CaCl_2$ solutions was also measured at smaller loads of 12 and 23 mN and the corresponding rates are summarized in Fig. 4c as a function of load (left for NaCl, and right for $CaCl_2$). The pressure solution rate becomes gradually more negative with an increase in normal load. The dissolution rate at a load of 47 nN is smaller in 1 mM NaCl compared to 0 mM and then it increases in 10 mM NaCl solution, but it is still smaller than in 0 mM. In contrast, a gradual addition of $CaCl_2$ enhances the dissolution rate, while the trend is inversed at high concentrations (100 mM and 1 M). It is to be noted that the effects of the brine composition on

the pressure-solution rate are greatly reduced at 23 mN in both solutions compared to 47 mN. In contrast, the influence of the fluid composition is relevant at a normal load of 12 mN, where an increase in calcite thickness with time, *i.e.* crystallization, was often measured, as illustrated by the positive pressure-solution rate. The positive pressure-solution rate coincides with the mineral precipitation within the contact area imaged by SEM, as discussed later.

3.3. Imaging of Pressure Solution Footprint

The footprint of pressure solution on the crystals was visualized by SEM at the end of the SFA experiments. Although initially the surfaces were smooth, significant surface roughening happened during pressure solution in NaCl, $CaCl_2$ and saturated $CaCO_3$ solutions. The first two rows in Fig. 5 show the images of two pairs of calcite crystals used in two different experiments in NaCl (Fig. 5a-e and f-j, corresponding to Fig. 4a and S5a, respectively). The following two rows (Fig. 5k-o and p-t) correspond to the images of two pairs of crystals used in the experiments with $CaCl_2$ solutions depicted in Fig. 4b and S5b, respectively. The SEM images of the corresponding unstressed regions that were immersed in the same saline solutions during the whole duration of the SFA experiment are shown in Fig. 5d, i, n, and s; they appear remarkably smoother at a similar magnification, which illustrates that the roughness within the contact area is significantly increased during pressure solution under all conditions compared to unstressed calcite.

Overall, the invasion of calcite is more prominent in NaCl solutions (Fig. 5a-b and f-g) than in $CaCl_2$ (Fig. 5k-l and p-q) and $CaCO_3$ solutions (Fig. 5v). The footprints show large networks of pits and grooves when pressure solution takes place in NaCl solutions, while the contact is relatively smoother but with elongated channels

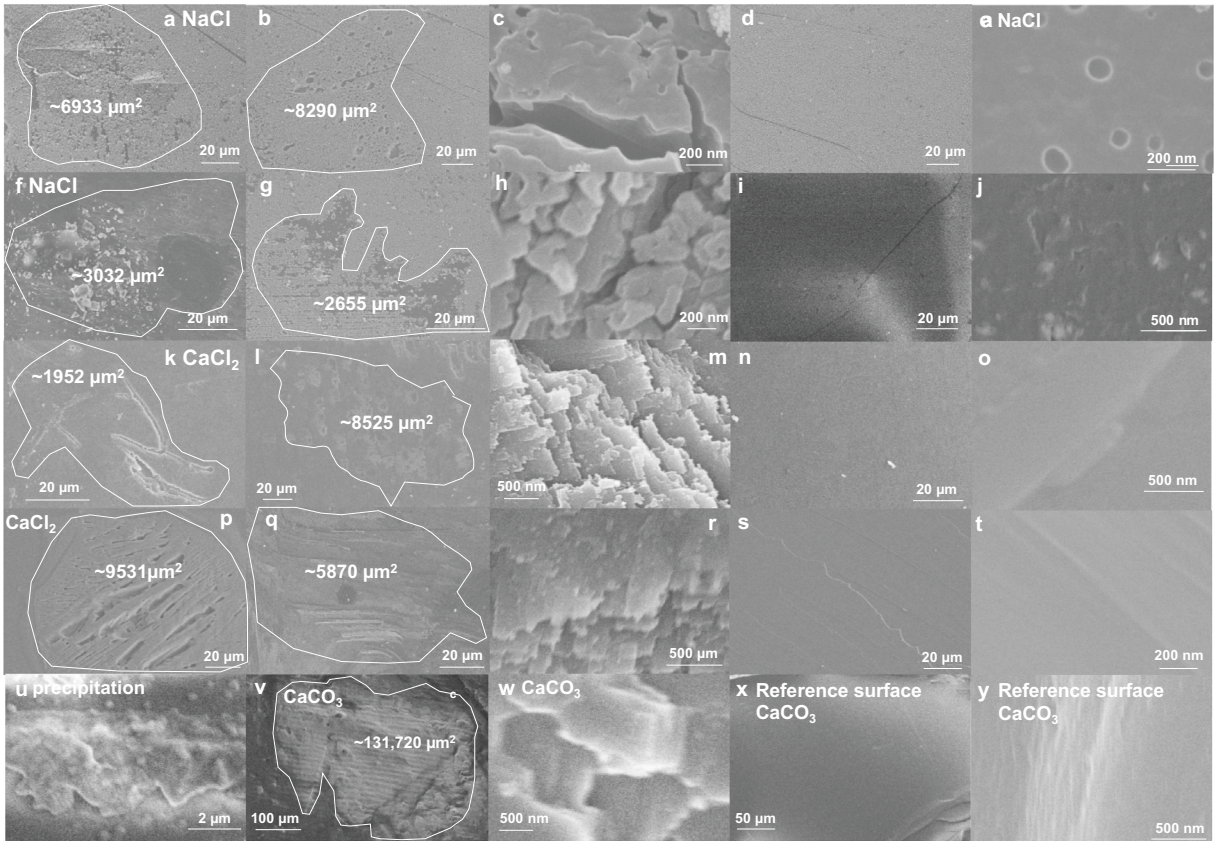

Fig. 5. SEM images of the footprints of pressure solution of calcite at the end of the SFA experiments. (a-t) SEM images of the calcite surfaces in a pair used in the same experiment, with the top two rows for 2 experiments in NaCl solutions, and the following two rows for $CaCl_2$. The white line in first and second columns shows the apparent contact region of each calcite pair. The third column shows the footprint at higher magnification, in comparison to the unstressed calcite surface, shown in the last two columns at low and high magnification, respectively. (u) illustrates the precipitation of calcite in the contact region. (v) shows the footprint of pressure solution in $CaCO_3$ saturated solution (Exp#2 in Fig. 2c), while (w) shows a higher magnification image. (x) and (y) shows two different magnifications of a calcite surface that was immersed in calcium carbonate saturated solution for 2 days as reference. Note that o, t, and y were taken in the vicinity of fortuitous steps, but the surfaces are overall flat without significant features. The apparent contact area (A) was estimated with ImageJ. In the SEM images, non-contact regions larger than a few microns were subtracted from A to provide an estimate of the true contact area A^* at the end of the experiment. Values for A^*/A are (a) 84%, (b) 85%, (f) 72%, (g) 83%, (k) 79%, (l) 88%, (p) 86%, (q) 91% and (v) 89%. This is a rough estimation of the true contact area because the size of the single-asperity contacts could be much smaller (of nanometer size).

in $CaCl_2$ and $CaCO_3$ solutions. Note that the concentration-specific roughening of calcite was not investigated, and hence, the influence of NaCl and $CaCl_2$ on the pressure-solution footprints represents the cumulative effects of solutions with concentrations from 1 mM to 1 M in both cases.

Higher magnification SEM imaging (Fig. 5c, h, m, r, and w) reveals further ion-specific differences in the pressure-solution footprint. At the nanoscale, dissolution leads to rounded features in NaCl solutions (Fig. 5c and h), while the rhombohedral shape of the crystal lattice is still retained in $CaCl_2$ solutions (Fig. 5m and r). The sharp features of the pressure solution footprints in $CaCO_3$ saturated solutions are similar to those in $CaCl_2$ solutions but of larger size (Fig. 5w). The most-right column in Fig. 5 show the images of unstressed calcite at a similarly high magnification. Only small and shallow pits are observed in NaCl (e and j), and the surfaces are almost featureless in $CaCl_2$ solutions (o and t), similar to the surface topography of unstressed calcite after long-immersion in saturated $CaCO_3$ solution (y).

Apparent and true contact areas (A and A^*) were estimated for each surface with software ImageJ and they ranged from 0.0017 to 0.013 mm^2 across the discussed experiments (Tables S5 and S6). Fig. 2d shows the pressure solution rates in saturated $CaCO_3$ solution as a function of the normal stress, which has been calculated as the average between $\sigma_n = F/A$ and $\sigma_n^* = F/A^*$ to represent the variation of the stress during the experiment; this calculation assumes that the contact area is reduced from A to A^* during the progress of pressure solution. In scenario b) (experiments #4–7), the dissolution rate was observed to increase with load, while Fig. 2d shows that the dissolution rate increases with stress in these experiments (empty markers). There is a clear but small deviation between the results from the different experiments in scenario b), which is attributed to the uncertainty about the real contact area. Fig. 5v shows the footprint in experiment #2 (scenario a), where pressure-solution rate decreased with increase in load. The contact area is estimated to be $A \sim 0.1$–0.13 mm^2 ($A^* \sim A{\cdot}0.89$), *i.e.* much larger than in experiments #4–7. As discussed later, this promotes a diffusion-controlled pressure solution.

The estimation of the stress also allows comparing results for pressure-solution in NaCl and $CaCl_2$ obtained in replica experiments. Overall, the pressure solution rate is much faster for NaCl brines in Fig. 4d compared to Fig. 4c, which is attributed to the higher normal stress in the former (up to 24 MPa *vs.* up to 7 MPa). Despite, this, at the highest normal stress in replica experiments (corresponding to 47 mN), the change in pressure solution rate due to a concentration change (of either NaCl or $CaCl_2$) is qualitatively similar, illustrating the qualitative agreement between results obtained with different pairs of calcite crystals. However, differences between replica experiments are observed upon a change in concentration of both salts at smaller normal stresses. For example, the highest precipitation rate in NaCl occurs at 10 mM in Fig. 4c (at ~ 2 MPa), while 10 mM NaCl yields the highest dissolution rate in Fig. 4d at a higher normal stress (5 MPa). In contrast, the precipitation rate in $CaCl_2$ in Fig. 4d is higher than in Fig. 4c although the estimated stress ($\sim$2 MPa) is of the same order of magnitude in both replica experiments. Here, the change in concentration of $CaCl_2$ does not lead to consistent changes in the precipitation rate in replica experiments. This lack of consistency across replica experiments at the smallest normal stresses seems to be related to the precipitation during pressure-solution of calcite.

3.4. Nanoindentation Tests in NaCl and $CaCl_2$ Solutions

Nanoindentation tests were performed to compare to the SFA experiments. Overall, the SFA results are in qualitative agreement with our nanoindentation experiments on calcite single crystals in the same brines at pressures ranging from 1 GPa to 3 GPa. At 1 mM NaCl, the indentation rate decreased in comparison to 0 mM, and the indentation rate gradually increased up to 100 mM NaCl, while a dramatic decrease was measured at 1 M NaCl. In the case of $CaCl_2$, the indentation rate increased with increase of the $CaCl_2$ concentration, except for 1 M $CaCl_2$. Cracks were observed in the SEM images of the indented regions, as demonstrated in Fig. 6b-c, likely due to the high tensile stresses in the indented region. Crack formation may have thus contributed to the measured indentation depth and the absolute values shown in Fig. 6a, which must, therefore, be considered with caution. In contrast, no cracks were detected in the SEM images after the SFA experiments, which is likely associated to the much smaller applied pressures (<25 MPa). Therefore, a quantitative comparison to the pressure solution rates measured with our SFA is not possible. While we do not aim to resolve the discrepancies between the two experimental methods, this comparison supports the feasibility of the extended SFA to study interfacial reactions of calcite single crystals.

4. DISCUSSION

4.1. Reaction-limiting step: diffusion vs. dissolution

Pressure solution consists of stress-induced dissolution of the mineral, ion diffusion through the fluid film trapped between the confining surfaces, and mineral precipitation in less stressed regions. Whichever step exhibits the slowest kinetics limits the pressure solution rate. The solubility of the stressed mineral (c_p) is elevated due to the increased chemical potential of the solid, $\Delta\mu_s = V_m(\sigma_n - P_f)$, V_m being the molar volume of the mineral and P_f the pressure of the unconfined fluid (0.1 MPa, here). Assuming the solid–fluid equilibrium condition and that the surface normal stress is equivalent to the pressure of the fluid yields $c_p = c_0 \exp(\Delta\mu_s/RT) = c_0 \exp(V_m(\sigma_n - P_f)/RT)$.

Various models have been proposed to describe pressure solution at grain boundaries (Gratier et al., 2013). The dynamic roughness (DR) model assumes that the real contacts supporting stress are small and change from place to place as old contacts dissolve and new contacts form. These points of contact do not limit the transport; the limiting transport length is the radius of the total contact area (A). The images in Fig. 5 suggest that the true contact area is

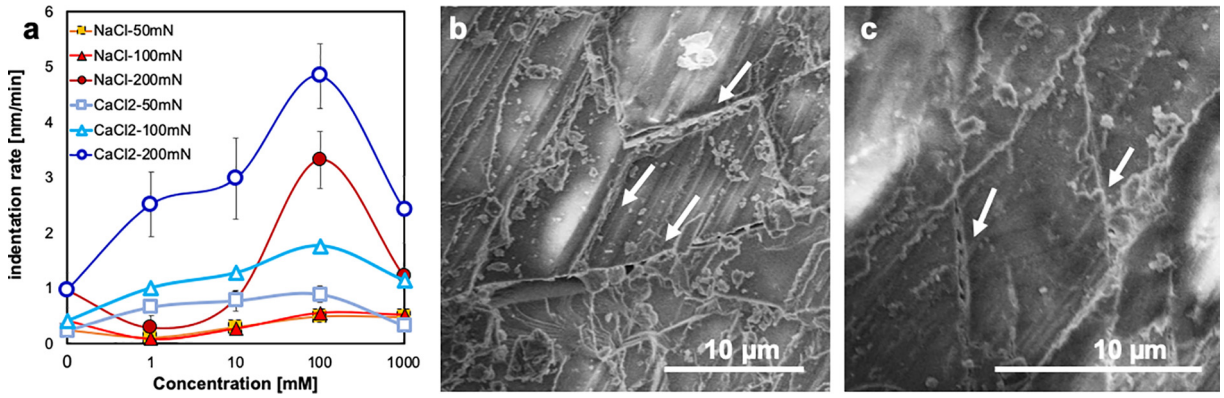

Fig. 6. (a) Indentation rates on calcite immersed in NaCl (red) and $CaCl_2$ (blue) solutions at the selected concentrations of 0 mM (no added salt, $CaCO_3$-saturated solution), 1 mM, 10 mM, 100 mM, and 1 M at applied loads of 50 mN, 100 mN, and 200 mN. The normal stress ranges from 1 GPa to 3 GPa in this range of loads. (b-c) SEM images of the indented region on two different calcite samples taken after the indentation tests to examine microcrack formation.

large, though ($A^* \gtrsim 0.8A$). Therefore, the footprints in Fig. 5 are more consistent with the island-channel network (Gratz, 1991). Here, the transport is limited by the diffusion in the thin fluid film trapped between contacting islands, which also support the stress. In this case, the rate-limiting transport length is the average island size (a), that is either a constant or increases with time (coarsening) (Dysthe et al., 2003a).

The diffusion-limited pressure-solution rate can be thus described as $\dot{r}_t \sim \mathbb{D} D c_p / a^2$, where $\mathbb{D}$ is the diffusion coefficient, D the thickness of the confined fluid film between the calcite surfaces, and a the limiting diffusion length. At stresses smaller than 30 MPa, like those estimated in this work, it is a good approximation to linearize the relation between c_p and $\Delta\mu_s$, so that $\dot{r}_t \sim \mathbb{D} D c_0 \Delta\mu_s / (RTa^2)$ (Zubtsov et al., 2005), and hence, the rate scales linearly with the normal stress. In contrast, if pressure solution is dissolution-limited, its rate scales with solubility$c$, that is, $\dot{r}_d \sim k(c_p - c_0)/c_0$, which can be approximated by $\dot{r}_d \sim k c_0 \Delta\mu_s / RT$ if $\sigma_n < 30$ MPa. A comparison to the data from (Zubtsov et al., 2005) demonstrates that this, in fact, is a good approximation for this work. This is illustrated in Fig. S6 in the SI. Zubtsov et al. measured a pressure-solution rate of -0.34 ± 0.11 nm/min at $\sim$ 100 MPa, which follows a quasi-linear relation with stress considering our results in Fig. 2d (experiments #4, #6 and #7, $R^2 \geq 0.98$, Fig. S6). It is worth emphasizing that the normal stress based on the footprint area A^* inferred from the SEM images likely underestimates the true stress at the asperity contacts since it does not account for the nanoscale roughness. Furthermore, these images were collected at the end of the experiment, and hence, the gradual change of contact area with load as the roughness evolved was ignored in this estimation of the normal stress. The current limitation of our experimental method to determine the evolution of the true contact area during the experiment does not allow us doing a more precise estimation. The error bars of the normal stress account partially for this uncertainty based on the difference between A and A^*. Despite these important limitations, these results appear to be consistent with a linear relation between stress and pressure-solution rate.

Two different scenarios for the pressure solution of calcite were observed in $CaCO_3$-saturated water. The scenario a (experiments #1 to #3 in Fig. 2c), *i.e.* when the dissolution rate slows down as the normal stress increases (and despite the increase in solubility), can be justified by diffusion-limitation. The ease of diffusion is characterized by $\mathbb{D} D / a^2$. Therefore, the observed decrease in rate with increase in stress could be justified by the decrease in fluid film thickness (D) and/or diffusion coefficient ($\mathbb{D}$), and/or by the increase in diffusion length (a).

Based on the theory of colloidal forces (Israelachvili, 2011) and supported by surface-force measurements on calcite (Røyne et al., 2015), a disjoining pressure is expected between *smooth* calcite surfaces in close proximity due to the action of surface forces, *i.e.* van der Waals, electrical double layer, and (strong) hydration forces in $CaCO_3$-saturated solutions. Such disjoining pressure prevents the direct contact between smooth surfaces so that a thin film of solution remains trapped between them. As the normal load is increased to $F \sim 12$ mN ($\sigma_n \sim 2$–6 MPa in experiments #4 to #6), the fluid film is partially squeezed out so that the film thickness decreases at the asperity contacts. Our previous force measurements by AFM with a silica colloid on calcite showed that the thickness of the fluid film is $D \sim 2$ nm (Diao and Espinosa-Marzal, 2016). While these AFM measurements did not reveal the surface force for calcite-calcite systems, we were able to disentangle the role of calcite on the hydration force through comparison to silica-silica measurements. Upon an increase in pressure to $\sim$ 20 MPa, our AFM experiments did not detect any further decrease in film thickness. This comparison revealed the action of a strong hydration force provided by the calcite surface that could justify the presence of a fluid film trapped at single asperity calcite contacts and capable of withstanding stress (Gratier et al., 2013). Consistent with this conclusion, molecular dynamic simulations have shown that four layers of water remain confined between two cal-

cite surfaces up to pressures of ~ 1 GPa (Brekke-Svaland and Bresme, 2018), two layers of water on each surface, which corresponds to a film thickness of$D \sim 1$ nm. Admittedly, the contact area is significantly roughened and a network of pits and grooves forms (Fig. 5), which leads to variations of the film thickness within the contact region. According to the island-channel network, the fluid film of a few nanometers in thickness confined at multi-asperity contacts ultimately limits the diffusion, and thereby, the pressure solution. On the other hand, it has been shown that the diffusion coefficient of water, sodium and calcium ions decreases by about two orders of magnitude in a 2-nm thin film compared to bulk diffusion, when confined between mica surfaces (Alcantar et al., 2003), or even more in silica nanopores (27). While a precise estimation is not possible yet, these and other studies support that the diffusion coefficient may be reduced at the asperity contacts between the calcite surfaces, as well. Nevertheless, neither D nor $\mathbb{D}$ are expected to decrease substantially with an increase in normal load from 12 to 47 mN ($\sigma_n \sim$ 1–25 MPa), and hence, it is unlikely that they are responsible for the two scenarios illustrated in Fig. 2a and b.

Importantly, the apparent contact area corresponding to the scenario in Fig. 2a (*e.g.* experiment #2) is at least 10 times larger than that in the experiments where the pressure-induced dissolution rate was observed to increase with stress (scenario b); see Tables S5 and S6. This suggests that the longer diffusion length through the network of pits and grooves could slow down the pressure solution of calcite in scenario a. Furthermore, the pressure-solution rate did not reverse as the load was decreased in this case (see Fig. 3a), which supports an irreversible change in the contact area (and diffusion length) during the experiment. Despite the uncertainty about the evolution of the contact area, and therefore of the contact stress, the relation between pressure-solution rate and apparent normal stress in Fig. 2d for this scenario (green full markers, see inset) is consistent with diffusion-limited pressure solution. On the other hand, if the diffusion length is small enough, the trapped solution travels sufficiently fast through the shorter (tortuous) pathway to less stressed regions and precipitates there, which decreases the local supersaturation in the contact and drives subsequent dissolution. This may lead to the dissolution-limited pressure solution of calcite and is consistent with the scenario b shown in Fig. 2d, *i.e.* with the increase in dissolution rate with the apparent normal stress. Note that in this case, the dissolution rate reversed when the load was decreased (see an example in Fig. 3b for scenario b), supporting that the change of the contact area during these experiments was less significant than the expected change of the solubility with pressure. Admittedly, the true contact area evolves significantly during the experiments, but the results in scenario b clearly deviate from the behavior in scenario a and can be explained by different limiting mechanisms for pressure solution.

SFA experiments were conducted on each pair of calcite crystals by gradually reducing the load (*i.e.* from 47 mN to 23 mN and then to 12 mN) in the selected brine while keeping the two surfaces in contact. An increasing crystal thickness over time (*i.e.* a positive pressure-solution rate in Fig. 2c and d) was measured occasionally at the smallest applied load of 12 mN, which implies that the precipitation of calcite happened within the contact region, as confirmed by SEM (Fig. 5u). According to thermodynamics, the gradient of chemical potential between the solution and the stressed calcite crystal must exceed zero for crystallization to happen, *i.e.* $\mu_{crys} = RT \ln(\sigma) > 0$, where $\tilde{\sigma}$ is the supersaturation of the fluid film (De Yoreo, 2003). This requires that the confined fluid film between the two calcite crystals becomes supersaturated with respect to the solubility of the stressed region ($c > c_p$). For growth to happen under an applied pressure, the supersaturation must fulfill $\tilde{\sigma} > \exp(V_m \sigma_n / RT)$ (Steiger, 2005). Using the normal stress (σ_n^*) to estimate the supersaturation yields that $\tilde{\sigma}$ must exceed 1.03 in the confined fluid at 12 mN. The crystal may also grow in the groves and pits, if $\tilde{\sigma} > 1$. The excess of ions in the confined fluid film could stem from the stress-induced dissolution of calcite at the preceding higher loads, as the dissolved mineral might remain in the trapped fluid phase and lead to the supersaturation of the solution when the stress is partially released; therefore, this process should be dependent of the loading history. The cartoon in Fig. 7a illustrates the relevance of surface-roughening and of the complex network of pits and grooves in dictating the pressure solution pathway.

The origin of surface roughening of minerals during dissolution has been amply discussed in the literature (Arvidson et al., 2003). The dissolution of the $(10\bar{1}4)$ cleav-

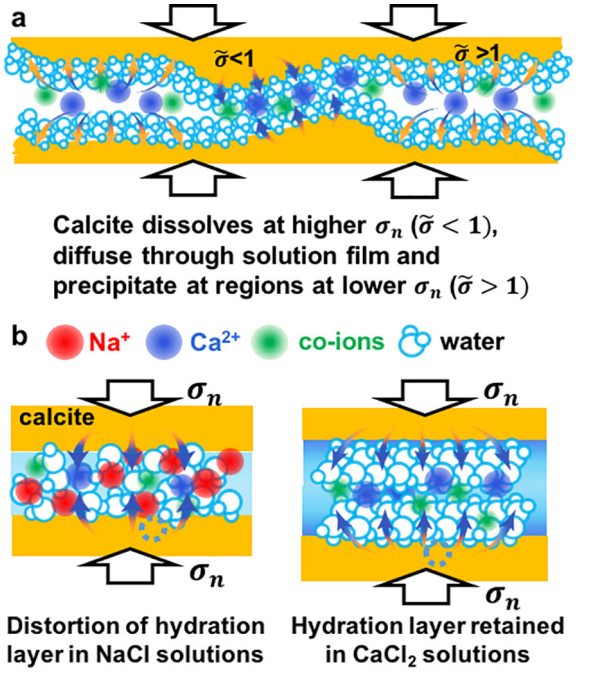

Fig. 7. Insights into the mechanisms underlying the pressure solution of calcite. (a) Excess of ions in the trapped fluid causing precipitation under applied pressure (σ_n and $\tilde{\sigma}$ represent apparent normal stress and supersaturation, respectively). (b) Na^+ and Ca^{2+} specific effects on pressure solution due to changes of the confined interfacial structure.

age plane of (unstressed) calcite happens through the development of a large diversity of coevolving reactive surface features, ranging from nucleation, growth and annihilation of shallow pits at dislocations (nm), long term development of complex, deep screw dislocations (>1 μm) and supersteps (~1 μm) (Bibi et al., 2018). This, along with the precipitation described earlier, leads to the roughening of the surface of calcite during pressure solution (Dziadkowiec et al., 2018). On the other hand, a destabilization of stressed mineral surfaces leading to immediate roughening (known as the Asaro-Tiller-Grinfeld instability) first (Asaro and Tiller, 1972; Grinfeld, 1986), and then followed by coarsening and smoothening due to the incorporation of dislocations during growth (Dysthe et al., 2003b) can also occur. The model predicts the instability to occur if the two solid surfaces have different dimensions or elastic properties. In the symmetric calcite-calcite systems of this study, such instability seems to be less likely, although we cannot completely exclude it.

4.2. Influence of Fluid Composition on Pressure Solution Kinetics

This work also provides evidence for the influence of the fluid composition on the pressure-solution rate of calcite. Interestingly, it is generally accepted that increasing ionic strength of the solution leads to an increase in the solubility of calcite, because the ion activity in solution is reduced due to stronger electrostatic interactions (Plummer, 1975). More specifically, it has been experimentally demonstrated that the solubility of stress-free calcite increases with NaCl concentration at concentrations below 1 M (Singurindy et al., 2004). This is, however, not obvious under the stress conditions provided in our experiments, perhaps because the confined *calcite-solution interface* exhibits a composition that differs from that of the unconfined interface. NaCl prohibits pressure solution at 1 mM and 10 mM compared to 0 mM, but it promotes pressure solution at 100 mM. In contrast, $CaCl_2$ promotes pressure solution from 1 to 100 mM compared to 0 mM. We propose that the ion-specific composition of the *calcite-solution interface* affects the pressure-solution rate. Our previous AFM studies (Diao and Espinosa-Marzal, 2019) and MD simulations (Ricci et al., 2013) have shown that sodium ions loose part of their hydration shell and penetrate and deteriorate the hydration layers of calcite; whereas the strongly hydrated calcium ions remain above the hydration layers and do not disturb them significantly (Fig. 7b). This should lead to a lower water content at the calcite-solution interface in NaCl compared to $CaCl_2$. The smaller interfacial amount of hydration water in NaCl might slow down the dissolution of calcium carbonate and outcompete the influence of the increase in ionic strength. This competition could explain the non-monotonic trend of the pressure-solution rate in NaCl solutions.

The SEM images also reflect the influence of the fluid composition. The footprints of pressure solution are similar in $CaCl_2$ and $CaCO_3$ solutions, both showing elongated channels with angular edges delineating the crystal lattice of calcite. The nanoscale features in $CaCl_2$ solutions suggest a more active surface reconstruction in the presence of higher near-surface calcium concentrations compared to saturated $CaCO_3$ solution. Note that our prior studies of the influence of $CaCl_2$ solutions on the dissolution of unstressed calcite (by AFM) showed pit formation at low concentration (Diao and Espinosa-Marzal, 2018). However, when the concentration was increased to 100 mM, enhanced surface reconstruction was revealed; and this became more prominent at 1 M. Such surface reconstruction is consistent with the SEM images shown in Fig. 5m, r and v. In the case of NaCl, Zhang et al. reported that the dissolution of the $(10\bar{1}4)$ cleavage of calcite was characterized by a dense distribution of etch pits and by the deepening of these dislocations at concentrations < 0.8 M (Zhang et al., 2009). Note that complex networks of pits and grooves are observed in the SEM images for NaCl at the μm-scale, strongly deviating from the footprint of the pressure solution of calcite in $CaCl_2$ solutions. This could be associated with the distortion of the hydration structure of calcite by the sodium ions described above, but more investigations are needed to prove this hypothesis. A closer look shows smoother and rounded edges, which might arise from the local precipitation of the trapped solute that has to travel along more tortuous and longer pathways, but this still remains speculative. Note that the surface flattened in Zhang et al.'s experiments above 0.8 M NaCl, with fewer (but well-defined) rhombohedral shape etch pits. The SEM images are the result of the convolution of the pressure solution at various concentrations, and hence, it is not possible to distinguish the influence of each single concentration. This calls for more systematic SFA studies of the surface roughening.

The results of this work let us also reconcile an apparent contradiction in the literature. Zhang and Spiers (Zhang and Spiers, 2005a) found that NaCl enhanced the compaction rate of granular calcite compared to $CaCO_3$-saturated solution, supporting that NaCl promotes pressure solution. We cannot exclude that the discrepancy from our results could rely on the influence of the fluid chemistry on other deformation mechanisms that contributed to the overall compaction rate of calcite gouge in Zhang's experiments, like subcritical crack growth. However, Zhang and Spiers (2005a) only investigated high NaCl concentrations, that is, 100 and 400 mM, from which they concluded that increasing salinity promotes pressure solution. This, in fact, agrees with our results in 100 mM NaCl. We speculate that the promotion of pressure solution prevails only up to a critical concentration of ~ 500 mM while the prohibitive effect of high ion concentration would come into play at higher concentrations, justifying the decrease in pressure-solution rate observed at 1 M in our SFA experiments. In fact, Liteanu and Spiers (2009) also measured a decrease in compaction rate of granular calcite in 1 M NaCl solutions. We tentatively attribute the abnormality at 1 M to ion-ion correlations at high ionic strength (Kjellander and Marcelja, 1984; Kjellander and Marčelja, 1988), which enhance the adhesion between the two surfaces (Javadi and Royne, 2018) and reduce the gap width (D), but this still requires further investigation.

Finally, our recent investigations of the frictional characteristics of calcite's $(10\bar{1}4)$ plane have revealed that pressure solution may significantly reduce friction at sufficiently high contact stresses, a phenomenon denoted as "pressure solution facilitated slip" (Diao and Espinosa-Marzal, 2018). By calculating the activation energy for slip, it was concluded that this phenomenon is influenced by the fluid composition (Diao and Espinosa-Marzal, 2019). Namely, the pressure solution facilitated slip is energetically less favorable in NaCl solutions up to 100 mM, and more favorable in $CaCl_2$ solution below 1 M, both compared to $CaCO_3$ saturated solutions. The reduction of the friction force is consistent with the measured pressure solution rates here, *i.e.* that NaCl solutions hinder pressure solution of calcite while $CaCl_2$ promotes it at concentrations $\leq$100 mM. This implies that the influence of fluid composition on the friction force at high stresses may be attributed to the ion-specific effects on pressure solution.

5. CONCLUSION

In summary, a surface forces apparatus (SFA)-based approach has been developed and used to investigate the pressure solution of calcite single crystals in a chemically symmetric contact that resembles the boundary interfaces of carbonate-based rocks, while excluding the complexity of carbonate gouge systems. The high-resolution measurements with the extended SFA combined with scanning electron microscopy imaging reveal two mechanisms underlying the pressure-solution rate based on the contact size and the influence of the interfacial fluid composition on the kinetics of pressure solution. Our previous work demonstrated that pressure solution occurring at the fault planes may serve as a potential weakening mechanism of fault strength in the context of injection-induced seismicity. Here, we provide direct evidence that pressure solution can be modified by the interfacial fluid chemistry, emphasizing that the composition of the injected fluid should be considered in the prediction of fault lubrication and induced earthquakes. By replacing calcite, the pressure solution of other brittle minerals such as gypsum and halite can be readily understood.

ACKNOWLEDGEMENTS

This work was supported by the National Science Foundation under grant No. NSF EAR 18-56525 and research board of University of Illinois Urbana-Champaign (UIUC). We also thank the Research Experience for Undergraduates (REU) program at the CEE Department, UIUC for financially supporting Anqi Li. Mengwei Han is sincerely appreciated for his help on SFA and Binxin Fu for measuring the effect of acetone on adhesion. We also would like to give deep gratitude to Prof. Manfred Heuberger for fruitful discussions about the extension of the SFA.

AUTHOR CONTRIBUTIONS

Y.D. performed SFA and SEM experiments. A.L. performed nanoindentation experiments. R. M. E.-M. designed the research and supervised the undergraduate and graduate students. Y.D. and R. M. E.-M. analyzed the data and wrote the manuscript.

DECLARATION OF COMPETING INTEREST

The authors certify that they do not have any conflict of interest in the subject matter or materials discussed in this manuscript.

RESEARCH DATA

Research Data associated with this article can be access at https://doi.org/10.5281/zenodo.3360741.

APPENDIX A. SUPPLEMENTARY DATA

Supplementary data to this article can be found online at https://doi.org/10.1016/j.gca.2020.04.010.

REFERENCES

Alcantar N., Israelachvili J. and Boles J. (2003) Forces and ionic transport between mica surfaces: Implications for pressure solution. *Geochim. Cosmochim. Acta* **67**, 1289–1304.

Arvidson R. S., Ertan I. E., Amonette J. E. and Luttge A. (2003) Variation in calcite dissolution rates: A fundamental problem?. *Geochim. Cosmochim. Acta* **67** 1623–1634.

Asaro R. J. and Tiller W. A. (1972) Interface Morphology Development during Stress-Corrosion Cracking. 1. *Via Surface Diffusion. Metall Trans* **3**, 1789–2000.

Bibi Irsha, Arvidson Rol, Fischer Corneliu and Lüttge Andrea (2018) Temporal Evolution of Calcite Surface Dissolution Kinetics. *Minerals* **8**(6), 256. https://doi.org/10.3390/min8060256.

Brekke-Svaland G. and Bresme F. (2018) Interactions Between Hydrated Calcium Carbonate Surfaces at Nanoconfinement Conditions. *J. Phys. Chem. C* **122**, 7321–7330.

Chen S.-Y., Kaufman Y., Kristiansen K., Seo D., Schrader A. M., Alotaibi M. B., Dobbs H. A., Cadirov N. A., Boles J. R., Ayirala S. C., Israelachvili J. N. and Yousef A. A. (2017) Effects of Salinity on Oil Recovery (the "Dilution Effect"): Experimental and Theoretical Studies of Crude Oil/Brine/Carbonate Surface Restructuring and Associated Physicochemical Interactions. *Energ Fuel* **31**, 8925–8941.

Chester F. M. and Higgs N. G. (1992) Multimechanism Friction Constitutive Model for Ultrafine Quartz Gouge at Hypocentral Conditions. *J. Geophys. Res.-Solid Earth* **97**, 1859–1870.

Croizé D., Renard F., Bjørlykke K. and Dysthe D. K. (2010) Experimental calcite dissolution under stress: Evolution of grain contact microstructure during pressure solution creep. *J. Geophys. Res.*, 115.

De Yoreo J. J. (2003) Principles of Crystal Nucleation and Growth. *Rev. Mineral Geochem.* **54**, 57–93.

Diao Y. and Espinosa-Marzal R. M. (2016) Molecular insight into the nanoconfined calcite-solution interface. *Proc. Natl. Acad. Sci. USA* **113**, 12047–12052.

Diao Y. and Espinosa-Marzal R. M. (2018) The role of water in fault lubrication. *Nat. Commun.* **9**, 2309.

Diao Y. and Espinosa-Marzal R. M. (2019) Effect of Fluid Chemistry on the Interfacial Composition, Adhesion, and Frictional Response of Calcite Single Crystals—Implications for Injection-Induced Seismicity. *J. Geophys. Res.: Sol Ea.* **124**, 5607–5628.

Dickinson J. T., Park N. S., Kim M. W. and Langford S. C. (1997) A scanning force microscope study of a tribochemicalsystem: stress-enhanced dissolution. *Tribol. Lett.* **3**, 69–80.

Dysthe D. K., Renard F., Feder J., Jamtveit B., Meakin P. and Jossang T. (2003a) High-resolution measurements of pressure solution creep. *Phys. Rev. E* **68**.

Dysthe D. K., Renard F., Feder J., Jamtveit B., Meakin P. and Jøssang T. (2003b) High-resolution measurements of pressure solution creep. *Phys. Rev. E* **68** 011603.

Dziadkowiec J., Javadi S., Bratvold J. E., Nilsen O. and Royne A. (2018) Surface Forces Apparatus Measurements of Interactions between Rough and Reactive Calcite Surfaces. *Langmuir* **34**, 7248–7263.

Gratier J. P., Dysthe D. K. and Renard F. (2013) The Role of Pressure Solution Creep in the Ductility of the Earth's Upper Crust. *Adv. Geophys. Elsevier*, 47–179.

Gratz A. J. (1991) Solution-Transfer Compaction of Quartzites - Progress toward a Rate Law. *Geology* **19**, 901–904.

Grinfeld M. A. (1986) Instability of Interface between Nonhydrostatically Stressed Elastic Body and Melts. *Dokl Akad Nauk Sssr+* **290**, 1358–1363.

Gundersen E., Renard F., Dysthe D. K., Bjorlykke K. and Jamtveit B. (2002) Coupling between pressure solution creep and diffusive mass transport in porous rocks. *J. Geophys. Res.-Solid Earth* **107**, ECV 19–11-ECV 19–19.

Heuberger M. (2001) The extended surface forces apparatus. Part I. Fast spectral correlation interferometry. *Rev. Sci. Instrum.* **72**, 1700–1707.

Israelachvili J. N. (1973) Thin film studies using multiple-beam interferometry. *J. Colloid Interf. Sci.* **44**, 259–272.

Israelachvili J. N. (2011) *Intermolecular and Surface Forces*, third ed. Elsevier, Amsterdam.

Javadi S. and Royne A. (2018) Adhesive forces between two cleaved calcite surfaces in NaCl solutions: The importance of ionic strength and normal loading. *J. Colloid Interface Sci.* **532**, 605–613.

Kjellander R. and Marcelja S. (1984) Correlation and Image Charge Effects in Electric Double-Layers. *Chem. Phys. Lett.* **112**, 49–53.

Kjellander R. and Marčelja S. (1988) Inhomogeneous Coulomb fluids with image interactions between planar surfaces. III. Distribution functions. *J. Chem. Phys.* **88**, 7138–7146.

Liteanu E. and Spiers C. J. (2009) Influence of pore fluid salt content on compaction creep of calcite aggregates in the presence of supercritical CO2. *Chem. Geol.* **265**, 134–147.

Plummer L. N. (1975) Mixing of Sea Water with Calcium Carbonate Ground Water. In *Quantitative Studies in the Geological Sciences* (ed. E. H. T. Whitten). Geological Society of America, pp. 219–236.

Ricci M., Spijker P., Stellacci F., Molinari J. F. and Voitchovsky K. (2013) Direct visualization of single ions in the Stern layer of calcite. *Langmuir* **29**, 2207–2216.

Røyne A., Dalby K. N. and Hassenkam T. (2015) Repulsive hydration forces between calcite surfaces and their effect on the brittle strength of calcite-bearing rocks. *Geophys. Res. Lett.* **42**, 4786–4794.

Rutter E. and Elliott D. (1976) The kinetics of rock deformation by pressure solution. *Philos. Trans. Royal Soc. A*, 203–219.

Singurindy O., Berkowitz B. and Lowell R. P. (2004) Carbonate dissolution and precipitation in coastal environments: Laboratory analysis and theoretical consideration. *Water Resour. Res.*, 40.

Steiger M. (2005) Crystal growth in porous materials—I: The crystallization pressure of large crystals. *J. Crys. Growth* **282**, 455–469.

Verberne B. A., Spiers C. J., Niemeijer A. R., De Bresser J. H. P., De Winter D. A. M. and Plümper O. (2013) Frictional Properties and Microstructure of Calcite-Rich Fault Gouges Sheared at Sub-Seismic Sliding Velocities. *Pure Appl. Geophys.* **171**, 2617–2640.

Weyl P. K. (1959) Pressure Solution and the Force of Crystallization - a Phenomenological Theory. *J. Geophys. Res.* **64**, 2001–2025.

Wheeler J. (2010) Anisotropic rheology during grain boundary diffusion creep and its relation to grain rotation, grain boundary sliding and superplasticity. *Philos. Mag.* **90**, 2841–2864.

Zhang, X., Salemans, J., Peach, C.J., Spiers, C.J., 2002. Compaction experiments on wet calcite powder at room temperature: evidence for operation of intergranular pressure solution. Deform. Mech., Rheol. Tectonics: Curr. Status Future Perspect. 200, 29–39.

Zhang X., Putnis A., Putnis C., Spiers C. J. and Geoconsultants P. (2009) *Effects of salinity on the morphology of dissolution pits in calcite - implication for CO2 sequestration in carbonate rocks*. International Symposium of the Society of Core Analysts, The Netherlands, pp. 27–30.

Zhang X. and Spiers C. J. (2005a) Compaction of granular calcite by pressure solution at room temperature and effects of pore fluid chemistry. *Int. J. Rock Mech. Min.* **42**, 950–960.

Zhang X. M. and Spiers C. J. T. (2005b) Effects of phosphate ions on intergranular pressure solution in calcite: An experimental study. *Geochim. Cosmochim. Acta* **69**, 5681–5691.

Zubtsov S., Renard F., Gratier J. P., Dysthe D. K. and Traskine V. (2005) Single-contact pressure solution creep on calcite monocrystals. *Geol. Soc. Spec. Publ.* **243**, 81–95.

Associate editor: Jean-francois Boily